Available online at www.sciencedirect.com
ScienceDirect
Journal of Catalysis 245 (2007) 215–227
JOURNAL OF CATALYSIS
www.elsevier.com/locate/jcat

Model for NO_x storage/reduction in the presence of CO_2 on a Pt–Ba/γ-Al_2O_3 catalyst

C.M.L. Scholz, V.R. Gangwal, M.H.J.M. de Croon, J.C. Schouten *

Laboratory of Chemical Reactor Engineering, Eindhoven University of Technology, P.O. Box 513, 5600 MB Eindhoven, The Netherlands

Received 24 May 2006; revised 29 September 2006; accepted 8 October 2006

Abstract

We have constructed a global reaction kinetic model to better understand and describe the NO_x storage/reduction process in the presence of CO_2. Experiments were performed in a packed-bed reactor with a Pt–Ba/γ-Al_2O_3 powder catalyst (1 wt% Pt and 30 wt% Ba) with different lean/rich cycle timings. The model is based on a multiple storage sites mechanism and considers that fast NO_x storage occurs at surface barium sites, as determined by the reaction kinetics. Slow NO_x storage occurs at the semi-bulk and bulk barium sites, where diffusion plays a major role. It is assumed that surface, bulk, and semi-bulk sites differ not only in physical appearance, but also in chemical reactivity. The distribution of these sites is obtained from 9-h lean-phase and 15-h rich-phase cycling experiments and thermogravimetric analysis of fresh catalyst. The model adequately describes the NO and NO_2 breakthrough profiles during 9 h of lean exposure, as well as the subsequent release and reduction of the stored NO_x. Furthermore, the model is also capable of simulating transient reactor experiments with 240-s lean-cycle and 60-s rich-cycle timings.

Keywords: NO_x trap; Barium nitrate; Lean-burn; Model; NO_x storage; NO_x reduction; Emissions; NO_x storage and reduction

1. Introduction

The popularity of diesel and lean-burn engines is increasing due to their better fuel efficiency and lower emission of the greenhouse gas CO_2 compared with conventional gasoline engines. However, achieving oxidation of CO and hydrocarbons simultaneously with NO_x reduction in the exhaust is challenging for lean-burn engines, in which excess O_2 in the exhaust gas hinders the reduction of NO_x. One promising approach to reducing NO_x during lean exhaust operation is the use of NO_x storage reduction (NSR) catalysts [1]. The most widely investigated NSR catalytic systems are Pt-based oxidation catalysts, which contain barium as a storage component. Under fuel-lean conditions, with excess O_2, NO_x is stored on the barium as nitrites/nitrates. As the storage capacity of barium is saturated, the catalyst must be regenerated. For regeneration, extra fuel is injected, resulting in a fuel-rich period during which NO_x is released and reduced to N_2. Understanding the NSR mechanism is crucial for reducing catalyst regeneration times and preventing catalyst deactivation. Unfortunately, the NSR catalysts have shown serious deactivation in the presence of SO_2 [2].

The NSR process has been the focus of several kinetic studies (see [3] and references herein); however, there is no clear agreement on the steps by which NO_x storage occurs. It is generally believed that NO is first oxidized to NO_2 over Pt sites. NO_2 is stored in the form of barium nitrate [4–7]. NO_2 storage can also proceed via a disproportionation route, resulting in nitrate formation and NO release in the gas phase [4,5,8]. There is growing evidence that in the presence of O_2, NO can be stored directly as barium nitrite [4,9]. In addition, the contribution of direct NO storage increases with increasing barium loading [10]. Nitrites can be further oxidized into nitrates with NO_2 as an oxidizing agent [11–13]. Furthermore, several studies have aimed to gain insight into the effect of different reductants in the fuel-rich phase. James et al. found that CO facilitates $Ba(NO_3)_2$ decomposition, but not NO_x reduction [14]. However, H_2 enables both to occur with high conversion to N_2.

In general, three different time periods can be distinguished during fuel-lean exposure. In the first period, complete NO_x

* Corresponding author.
E-mail address: j.c.schouten@tue.nl (J.C. Schouten).
URL: http://www.chem.tue.nl/scr.

0021-9517/$ – see front matter
doi:10.1016/j.jcat.2006.10.011

storage occurs. During the second period, NO_x breakthrough with considerable NO_x storage is observed. The third period is characterized by slow NO_x storage and persists longer than the other two periods. The three different time periods indicate the presence of multiple types of barium sites with different reactivities toward NO_x storage [15]. Barium sites located close to Pt sites are considered more reactive than barium sites located farther away [16]. Barium can be present in the catalyst as BaO, $Ba(OH)_2$, and $BaCO_3$, depending on the reaction conditions [7]. NO_x storage occurs preferentially at BaO, then at $Ba(OH)_2$, followed by $BaCO_3$ sites. Recently, low-temperature (LT) and high-temperature (HT) barium-containing species have been distinguished [17,18]. The crystalline bulk-like HT-barium sites are thermally more stable than the well-dispersed LT-barium phase. The LT-barium sites show a higher activity toward NO_x storage and reduction than the HT sites [19,20]. With an increase in total barium loading, the number of LT sites initially increases, reaching a constant maximum value at a barium loading of about 17% (w/w) [18,19]. The HT phase also increases with barium loading, without saturation.

Although there is clear evidence in the literature that multiple types of barium sites exist, models of the NSR process are based mostly on a single type of reaction site. Olsson et al. [21] developed an elementary kinetic model, but this model could not describe the decreasing NO_x trapping activity observed as the lean phase proceeded. Global models based on shrinking core mechanisms have been used to describe the NO_x storage process [22–25]. In general, these models assume that NO_x diffusion inside the barium clusters or NO_x transfer to the barium sites is the rate-controlling step in the NO_x storage process. The presence of an inactive barium core has been assumed to describe the observed incomplete barium utilization [23]. In all of these models, no distinction is made between reactivity of surface and bulk barium sites toward NO_x storage.

Furthermore, the vehicle exhaust gas always contains CO_2 and H_2O. However, most studies do not take into account the presence of these species. It has been reported that CO_2 negatively affects the NO_x storage process [15,26,27], whereas NO_x release studies have shown that CO_2 has a promoting effect on NO_x release in the fuel-rich phase [26,28,29]. The H_2O effect is limited to the NO_x storage process mainly at low temperatures (below 300 °C) [26].

The goal of the present work is to develop a global reaction kinetic model based on a multiple–storage sites mechanism for the NSR process in the presence of CO_2. In addition, the model provides a better understanding of reaction steps and barium utilization during the NSR process at different time scales. Experiments have been performed in a packed-bed reactor with a Pt–Ba/γ-Al_2O_3 powder catalyst (1 wt% Pt and 30 wt% Ba) with different lean-cycle/rich-cycle timings. The contributions of the different barium sites and the model parameters have been deduced from 9-h lean-cycling/15-h rich-cycling experiments. The model was validated for other conditions, including different NO concentrations and different H_2 concentrations. In addition, cycle times of 240 s lean and 60 s rich have been used to demonstrate the applicability of the developed model for lean/rich timings under conditions more closely resembling automotive exhaust conditions. NO is used as the NO_x source, whereas H_2 is used as the reducing agent. Catalyst characterization using thermogravimetric analysis (TGA) combined with mass spectrometry (MS), XRD, BET analysis, and Pt dispersion measurement has been done to support the model results.

2. Experimental

2.1. Alternation of lean and rich flows

Lean/rich cycling experiments were performed in a packed-bed reactor, as described previously [30]. The gas composition of reactants and products was measured with an on-line quadrupole mass spectrometer (ESS). A fixed amount of argon was fed as an internal standard during experiments to compensate for any intensity loss of the mass spectrometer. Gas analysis was performed on m/e 2 (H_2), 17 ($NH_3 + H_2O$), 18 (H_2O), 28 ($N_2 + CO_2 + CO$), 30 ($NO + NO_2$), 32 (O_2), 40 (Ar), 44 ($CO_2 + N_2O$), and 46 (NO_2). A high-resolution magnetic sector mass spectrometer (Jeol JMS GCmate) was also used for the analysis of $N_2 + CO$ and $CO_2 + N_2O$. It was verified that external and internal diffusion limitations were absent at the scale of the catalyst pellet. A NO_x storage catalyst, Pt–Ba/Al_2O_3 (1/30/100 w/w/w), was used in powder form as provided by Engelhard. Typically, 1.9 g of catalyst with an average pellet diameter of 180 μm was used in the NO_x storage/reduction experiments. The fresh catalyst was pretreated at 773 K with 1 vol% of oxygen in helium for 1 h, followed by 0.5 h in helium, and finally by reduction with 2 vol% of hydrogen in helium for 2 h. The total gas flow during the experiments was kept constant at 0.743 mmol/s, resulting in a gas hourly space velocity (GHSV) of 29,000 h^{-1} (standard conditions, 298 K and 1 bar). Table 1 shows the experimental conditions for the lean/rich cycling experiments.

Table 1
Experimental conditions of lean/rich cycling experiments

	Temperature (K)	Inlet lean[a]	Inlet rich[a]
9 h lean/15 h rich	513, 573, 643	0.2 vol% NO 4 vol% O_2 10 vol% CO_2 1 vol% Ar	0.8 vol% H_2 10 vol% CO_2 1 vol% Ar
	573	0.3 vol% NO 4 vol% O_2 10 vol% CO_2 1 vol% Ar	0.8 vol% H_2 10 vol% CO_2 1 vol% Ar
	573	0.2 vol% NO 4 vol% O_2 10 vol% CO_2 1 vol% Ar	1.2 vol% H_2 10 vol% CO_2 1 vol% Ar
4 min lean/1 min rich	573	0.2 vol% NO 4 vol% O_2 10 vol% CO_2 1 vol% Ar	0.8 vol% H_2 10 vol% CO_2 1 vol% Ar

[a] He is carrier gas.

Table 2
BET surface area, pore volume and Pt dispersion[a]

	BET (m^2/g)	Pore volume (cm^3/g)	Pt dispersion (%)
Fresh	71	0.22	
Pretreated	70	0.22	20 ± 1
After lean, with CO_2	70	0.22	20 ± 1
After rich, with CO_2	70	0.22	20 ± 1

[a] Lean exposure: 9 h, 0.2 vol% NO, 4 vol% O_2, 10 vol% CO_2 and 1 vol% Ar. $T = 573$ K. Rich exposure: 15 h, 0.8 vol% H_2, 10 vol% CO_2 and 1 vol% Ar. $T = 573$ K.

In practice, CO and hydrocarbons make up a significant portion of the reductant in the fuel-rich phase. However, quantification of the data with H_2 as a reductant is less complicated, because H_2 shows no mass overlap at m/e 28; thus, H_2 was used in this study. H_2 was fed at higher concentrations as typically present in a real exhaust gas, to ensure complete catalyst regeneration. NO was also fed at higher concentrations to guarantee sufficient sensitivity of the mass spectrometer for the gas-phase component NO_2. The other experimental conditions are representative for conditions in diesel and lean-burn exhaust gases.

2.2. Catalyst characterization

Surface area, pore volume, and pore size distribution were determined in fresh catalyst samples and catalyst samples used in the lean/rich cycling experiments. Samples used in the lean/rich cycling experiments were obtained after the cyclic steady state had been reached. The surface area was determined with the BET method at 77 K with N_2 as the adsorbent using a Tristar instrument (Micromeritics). The BJH pore size distribution and pore volume were calculated from the N_2 desorption isotherm. Pt dispersion was obtained from CO chemisorption at 298 K using an ASAP-2000 instrument (Micromeritics) and determined for pretreated catalyst samples and catalyst samples used in lean/rich cycling experiments. The BET surface area, pore volume and Pt dispersion are given in Table 2.

Powder X-ray diffraction was done with a Rigaku Geigerflex diffractometer. Typically, an XRD spectrum was recorded in the range $15° < 2\theta < 75°$ using Cu$K\alpha$ radiation. Thermogravimetric analysis (TGA) was carried out using a TGA/DSC (Mettler-Toledo) setup combined with mass spectrometry (Quadrupole MS, Pfeiffer Vacuum). A 50-mg catalyst sample and a 30-ml/min flow of pure He were used with a heating rate of 10 K/min.

3. Results

Fig. 1 presents typical results obtained during lean/rich cycling experiments with 9 h of lean flow and 15 h of rich flow at 573 K. The data shown were collected after three storage/reduction cycles when the cyclic steady state had been reached. The NO_x breakthrough profile shown in Fig. 1a can be divided in three time periods. In the first period of the lean phase, complete NO_x storage is seen. The second period starts after 6.2 min as NO breakthrough is observed. The NO outlet concentration reached a maximum value after 42.5 min, at

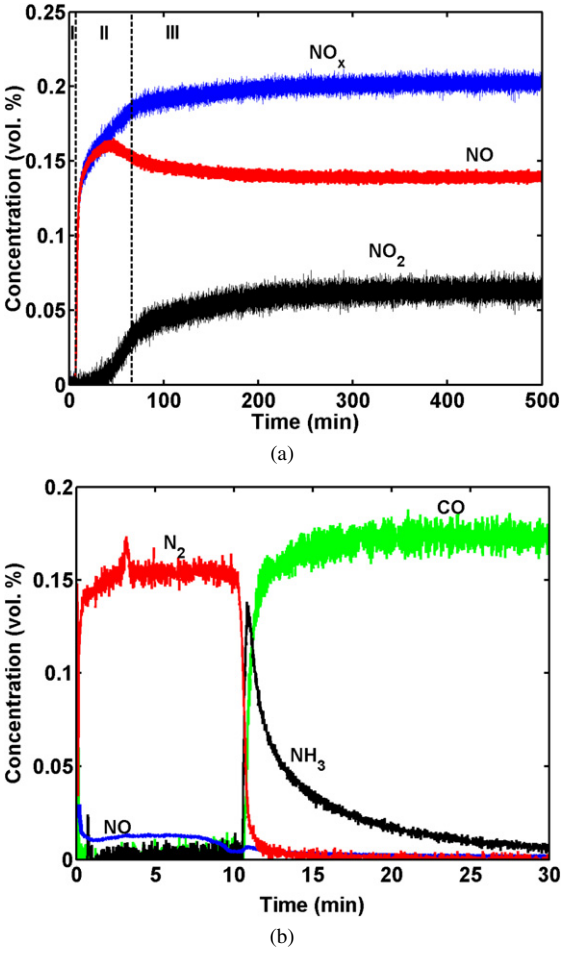

Fig. 1. (a) Lean outlet concentrations of NO, NO_2 and NO_x at cyclic steady state. Lean phase: 0.2 vol% NO, 4 vol% O_2, 10 vol% CO_2 and 1 vol% Ar, 9 h. Three different time periods can be distinguished. (b) Rich outlet concentrations of N_2, NH_3, NO and CO at cyclic steady state. Rich phase: 0.8 vol% H_2, 10 vol% CO_2 and 1 vol% Ar, 15 h. $T = 573$ K.

which point the NO concentration began to decrease. Meanwhile, during the first 33.3 min, NO_2 was completely consumed. After 33.3 min, the NO_2 concentration increased with time. During the first 65 min of the lean phase, there was still considerable NO_x storage. The third period (>65 min) is characterized by a slow but still measurable uptake of NO_x until 200 min. After 200 min, the NO_x concentration was constant and equal to the inlet concentration. Because there is no NO_x storage, the detected outlet 0.14 vol% NO and outlet 0.06 vol% NO_2 concentrations can be ascribed to the NO oxidation reaction.

If NO_x were stored through the disproportionation route only, then the disproportionation stoichiometry should be observed. This stoichiometry implies that for every three molecules of NO_2 removed from the gas phase, two molecules of NO_x are stored on the barium and one molecule is released in the form of NO. It is assumed that the NO oxidation reaction is very fast and that the NO and NO_2 concentrations in the gas phase correspond to the oxidation reaction. Fig. 2 shows the measured NO concentration and the calculated NO concentration as determined by the disproportionation mechanism:

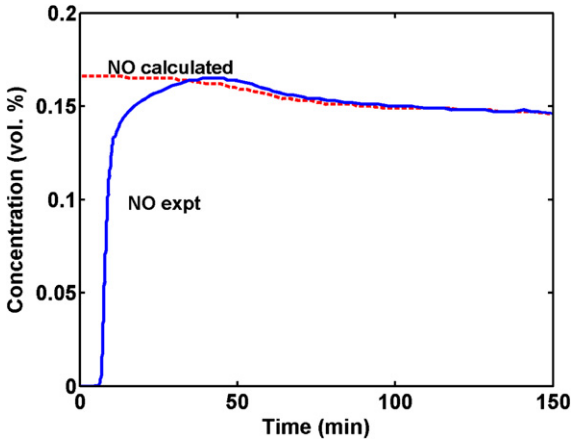

Fig. 2. NO outlet concentration and calculated NO concentration according to the disproportionation mechanism. For experimental conditions, see Fig. 1.

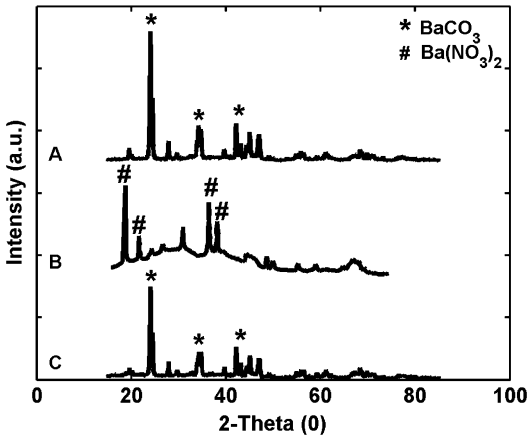

Fig. 3. XRD patterns of (A) fresh catalyst, (B) after lean/rich cycling, ending with lean exposure (lean: 0.2 vol% NO, 4 vol% O_2 and 1 vol% Ar, 9 h), (C) after lean/rich cycling, ending with lean exposure (lean: 0.2 vol% NO, 4 vol% O_2, 10 vol% CO_2 and 1 vol% Ar, 9 h). In the presence of CO_2, even after 9 h lean exposure, no crystalline bulk $Ba(NO_3)_2$ is formed contrary to the results in the absence of CO_2.

Table 3
Barium utilization for lean and rich phases[a]

	Cycle no		
	1	2	3
Lean phase: % Ba active	32	31	32
Rich phase: % reduced	32	32	33

[a] Lean phase: 9 h, 0.2 vol% NO, 4 vol% O_2, 10 vol% CO_2 and 1 vol% Ar. Rich phase: 15 h, 0.8 vol% H_2, 10 vol% CO_2 and 1 vol% Ar. $T = 573$ K. See also Fig. 1.

calculated NO concentration $= 1/3 \times$ stored $NO_2 + 0.14$ vol%. As shown in Fig. 2, according to the disproportionation mechanism, immediate NO formation should be observed. However, no NO was seen during the first 6.2 min, indicating that initial NO_x storage occurred mainly through NO storage, that is, through nitrites. After 36 min, more NO was observed, as calculated through the disproportionation route. Thus, it is thus unlikely that NO_x was stored through the disproportionation route only. Nitrites are also oxidized into nitrates with NO_2 as the oxidizing agent [11–13]. As a result, mainly nitrates will be present after 9 h of lean exposure. In parallel, NO_2 also can be stored directly onto nitrates without NO release [4–7].

Barium utilization after 9 h of lean exposure corresponded to 32% of the total barium present assuming that 2 moles of NO_x were stored per mole of barium and assuming a negligible capacity of γ-Al_2O_3 for NO_x storage at 573 K [9]. Table 3 presents the barium utilization of the previous lean/rich cycles, showing the same fraction of barium active in NO_x storage. In addition, lean/rich cycling experiments in the presence of CO_2 at 513 and 643 K have also shown that about 30% of total barium is involved in the NO_x storage and reduction process. In a earlier paper [30], we reported that in the absence of CO_2, almost 100% of barium was involved in NO_x storage when the pretreated catalyst was exposed to 9 h lean conditions. It also has been reported that NO_x cannot be stored on bulk barium sites in the presence of CO_2 [31,32]. In addition, CO_2 competes with NO_2 for the same barium sites, inhibiting NO_x storage [15,26,27].

Fig. 3 compares the XRD pattern of the fresh catalyst with the XRD patterns of the catalyst exposed to lean/rich cycling experiments with and without CO_2 present in the gas feed. The XRD analysis of the fresh catalyst pattern (A) shows the presence of crystalline $BaCO_3$. Finely dispersed barium sites are invisible for XRD, whereas the bulk-barium phase is crystalline and detectable with XRD [18]. This suggests that the observed crystalline phase of the fresh catalyst corresponds to bulk $BaCO_3$.

After 9 h of lean exposure in the absence of CO_2 [pattern (B)], only peaks characteristic for crystalline $Ba(NO_3)_2$ can be seen, suggesting transformation of bulk $BaCO_3$ to bulk $Ba(NO_3)_2$. However, after 9 h of lean exposure in the presence of CO_2 [pattern (C)], only peaks characteristic for crystalline $BaCO_3$ can be seen; crystalline $Ba(NO_3)_2$ is not observed. This indicates that bulk $BaCO_3$ sites are inactive in the NO_x storage process in the presence of CO_2.

Fig. 4 shows the TG and DTG curves of the fresh catalyst. Three distinct thermal decomposition events are shown in the DTG curve, with peaks located at 1040, 1110, and 1273 K, respectively. This indicates the presence of three thermally different species. Piacentini et al. [18] found two thermal decomposition events for calcined catalysts. The low-temperature decomposition event is ascribed to the decomposition of LT-$BaCO_3$ to BaO, and the high-temperature event is associated with the decomposition of the HT-$BaCO_3$ sites. Nevertheless, three different barium species are distinguished: amorphous BaO, amorphous LT-$BaCO_3$, and crystalline HT-$BaCO_3$. The thermal stability of these species depends on their interaction with the alumina support and Pt sites. As the catalyst is exposed to the atmosphere, BaO will react with atmospheric CO_2 to form $BaCO_3$ with low thermal stability [18]. The catalyst in the present study was stored for 3 years under ambient atmosphere, and most of the barium was present as $BaCO_3$. This might explain why the DTG curve shows three weight loss events. The first two events are ascribed to the decomposition of a dispersed LT phase. The HT event is ascribed to the decomposition of crystalline, bulk HT barium sites. The evolving gases

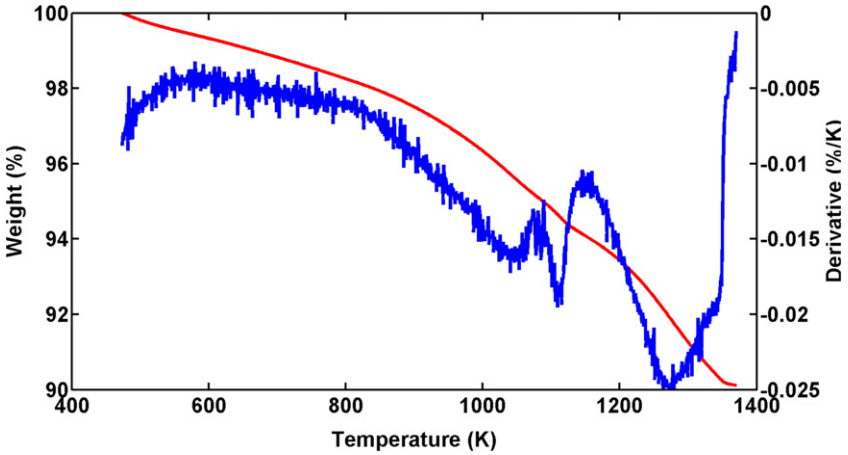

Fig. 4. TG-DTG curve for the thermal decomposition of fresh catalyst.

during this TG experiment were analyzed by mass spectrometry. The MS signal (not shown) shows three evolution events, with peaks located at the same temperatures as for the TG measurement. The evolving gas above 600 K for all three events is CO_2. We used a curve-fitting procedure for the CO_2 MS signal to calculate the integrals of the peaks. This shows that the relative LT weight loss is 35%, whereas the HT weight loss is 65%. This distribution of amorphous LT sites and crystalline HT sites corresponds well with the results of the lean/rich cycling experiments (30% LT sites and 70% HT sites), in line with observations in the literature [19].

The fuel-rich phase is shown in Fig. 1b. On switching from lean to rich conditions, immediate N_2 formation and NO release can be seen. Minor amounts of NO_2 are detected. NO_x is formed through nitrite/nitrate decomposition, as mentioned by Lietti et al. [7]. The released NO_x is reduced to N_2 on the Pt sites. During N_2 formation, H_2 is completely consumed (not shown). Mahzoul et al. [16] concluded that two reduction processes proceed in parallel: reduction of stored NO_x and reduction of oxidized Pt sites. This agrees with our experimental data. In the beginning of the fuel-rich phase, part of the fed hydrogen is used for the reduction of the oxidized Pt sites. This leads to less available hydrogen for the reduction of the released NO_x, resulting in a lower N_2 concentration. When the oxidized Pt sites are reduced, more hydrogen and Pt sites are available for reduction of the stored NO_x. At that time, the N_2 concentration increases to 0.15 vol% corresponding to that expected from nitrate reduction. NH_3 and CO formation is observed once the N_2 production declines. The CO formation is accompanied by the parallel consumption of H_2 and CO_2 and parallel production of H_2O (not shown). This suggests that the reverse water-gas shift (WGS) reaction takes place. The NH_3 formation indicates that the selectivity toward N_2 decreases with time, which seems to coincide with the diminishing quantity of NO. The N balance shows that the NO_x stored during the fuel-lean phase is completely regenerated during the fuel-rich phase. Closed N balances are also observed in the preceding lean/rich cycles (Table 3), and there are no signs of incomplete regeneration.

4. Modeling

4.1. Kinetic model construction

The experimental results show that initially in the lean-phase fast NO_x storage occurs on Ba sites, followed by slow storage. Not all of the Ba sites participate in the NO_x storage process and approximately 70% of Ba remains inactive. As discussed above, in the presence of excess CO_2, barium is present mainly in the carbonate form.

The three thermal events seen in the TGA, as discussed in the previous section, confirm the presence of three types of storage sites. The first thermal event is associated with surface Ba-sites, where fast NO_x storage occurs. The storage process is determined by the reaction kinetics. The second and third events are associated with the semi-bulk and bulk Ba sites, respectively. At these sites, slow NO_x storage takes place, which is limited by NO_x diffusion inside the barium cluster. The surface, semi-bulk, and bulk sites differ not only in physical appearance (as shown in Fig. 5), but also in chemical reactivity; surface sites are the most reactive, and bulk sites are the least reactive. This is in line with Piacentini et al. [18] who suggested that depending on the Ba loading, three types of Ba species, which differ in reactivity and particle size, exist on the support.

The surface sites are also present as highly dispersed barium carbonate species (not shown) along with Pt sites. The total amount of the surface barium and Pt sites affects the model results. The global reaction steps and rate equations used for

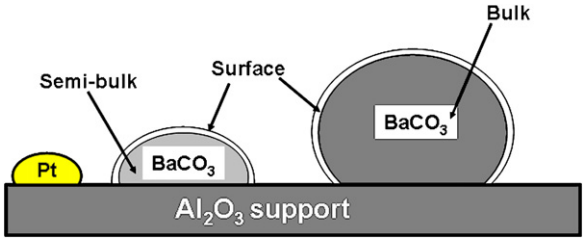

Fig. 5. Pictorial representation of surface, semi-bulk and bulk barium sites. Surface and semi-bulk sites are amorphous LT-sites. Bulk sites are crystalline HT-sites.

Table 4
The global reaction steps and rate equations used for modeling NO_x storage and reduction[a]

Reactions	Rate equation	
Lean phase		
$NO + 0.5O_2 \Leftrightarrow NO_2$	$R_{ox} = k_{ox\_f} C_{NO} C_{O_2}^{0.5} - k_{ox\_b} C_{NO_2}$	(I)
$BaCO_3 + 2NO + 0.5O_2 \rightarrow Ba(NO_2)_2 + CO_2$	$R_{st\_NO} = k_{s\_NO,i} \theta_{BaCO_3,i} C_{NO}^2 C_{O_2}^{0.5}$	(II)
$Ba(NO_2)_2 + 2NO_2 \rightarrow Ba(NO_3)_2 + 2NO$	$R_{st\_oxi} = k_{s\_dis,i} \theta_{Ba(NO_2)_2,i} C_{NO_2}^2$	(III)
$BaCO_3 + 2NO_2 + 0.5O_2 \rightarrow Ba(NO_3)_2 + CO_2$	$R_{st\_NO_2} = k_{s\_NO_2,i} \theta_{BaCO_3,i} C_{NO_2}^2 C_{O_2}^{0.5}$	(IV)
Rich phase		
$Ba(NO_2)_2 + H_2 + CO_2 \rightarrow BaCO_3 + 2NO + H_2O$	$R_{reg,nitrite} = k_{reg,nitrite,i} \theta_{Ba(NO_2)_2,i} C_{H_2}$	(V)
$Ba(NO_3)_2 + 3H_2 + CO_2 \rightarrow BaCO_3 + 2NO + 3H_2O$	$R_{reg,nitrate} = k_{reg,nitrate,i} \theta_{Ba(NO_3)_2,i} C_{H_2}$	(VI)
$NO + H_2 \rightarrow 0.5N_2 + H_2O$	$R_{red} = k_{red} C_{NO} C_{H_2}$	(VII)

[a] The reaction rate parameters $k_{s\_NO,i}$, $k_{s\_dis,i}$, $k_{s\_NO_2,i}$, $k_{reg,nitrite,i}$, and $k_{reg,nitrate,i}$ have different units and values for the surface, semi-bulk and bulk barium sites with i—surface, semi-bulk or bulk. See also Table 5.

modeling NO_x storage and reduction with surface, semi-bulk, and bulk barium sites are presented in Table 4.

An important reaction step in the NO_x storage mechanism is the oxidation of NO into NO_2 on the Pt sites. We use the same form for the corresponding global reaction rate as that published by Olsson et al. [23] [reaction (I), Table 4]. The experimental results show that the NO_x storage process is quite complex, and different routes are possible. In this modeling, NO_x storage is considered to occur through nitrite and nitrate formation. At first, NO will adsorb on the catalyst in the form of barium nitrites [4,9], as presented in reaction (II) (Table 4). These nitrites can be further oxidized to nitrates by NO_2, resulting in NO release [reaction (III), Table 4] [11–13]. NO_2 can be stored directly as barium nitrates [reaction (IV), Table 4] [4–6]. With these two steps (III + IV), the experimentally observed stoichiometry of NO released and NO_2 stored can be described well. As described before, the disproportionation route is not able to explain the measured NO concentration, and thus this step is not included.

In the fuel-rich phase, regeneration of barium sites is considered to take place through nitrite/nitrate decomposition, as mentioned by Lietti et al. [7], and as presented in reactions (V) and (VI) (Table 4). The released NO_x is reduced on the Pt sites into N_2 with the help of a reductant, described by reaction (VII) (Table 4). NH_3 formation is not taken into account, because no NH_3 is observed in the experiments with lean/rich cycling times close to automotive conditions. For the same reason, the reverse WGS reaction is not included. The activation energy for NO oxidation [reaction (I), Table 4] is taken from Olsson et al. [23]. The pre-exponential factor for the NO oxidation and the storage and reduction kinetic parameters are obtained by manually fitting the results of the model to the results of the 9-h/15-h lean/rich cycling experiments. The distribution of surface, semi-bulk, and bulk sites is also acquired from the 9-h/15-h lean/rich cycling experiment supported by the results of the TGA experiment; 73% of the total barium sites corresponds with bulk barium sites, 7% with surface barium sites, and 20% with semi-bulk barium sites. The diffusion coefficient of the gas-phase components in the semi-bulk and bulk barium is taken to be 3.6×10^{-15} m^2/s. Dong et al. suggested that the diffusion coefficient in the case of diffusion through the bulk of oxides is on the order of 10^{-16} m^2/s [33]. A semi-bulk barium cluster size of about 10 nm is obtained via CO_2 chemisorption. Calculations based on this value and on the fitted model parameters lead to a bulk barium cluster size of about 40 nm. This is in agreement with XRD results, which give a particle size range of 10–40 nm. Furthermore, a free alumina of 50.7 m^2/g of catalyst can be estimated. We expect that at 300 °C this alumina has <1.5% storage capacity for NO_x. This was verified by performing NO desorption experiments with pure γ-alumina (BET, 200 m^2/gm). The model parameters and constants are given in Table 5.

4.2. Reactor model

The packed-bed reactor is considered an ideal plug-flow reactor under isothermal conditions; experimental data show a maximum increase in temperature of 5 K. The model is constructed to describe NO_x storage and reduction at 573 K. The pressure is taken to be uniform and equal to ambient throughout the packed bed. External and internal diffusion limitations are absent. Diffusion of the gas-phase components is considered only from the external surface of the barium clusters to the interior of the barium clusters. The gas bulk in the packed-bed reactor is discretized in axial direction z, and the gas in the spherical barium clusters with the partial coordinate ξ. Both parts are connected with diffusion from the bulk gas to the inner side of the barium clusters. The change in the concentration of the different components as a function of time at each axial position can be described as follows:

$$\varepsilon_b \frac{\partial C_i}{\partial t} = -\frac{F_v}{A_r}\frac{\partial C_i}{\partial z} - D_{eff} A_{Ba} \left.\frac{\partial C_i}{\partial \xi}\right|_{\xi=R} + L_{Pt} \sum_j \upsilon_{i,j} R_{Pt,j} + L_{Ba,surf} \sum_k \upsilon_{i,k} R_{Ba\_surf,k}, \quad (1)$$

Accumulation of moles in gas phase | Convective flow transport through reactor | Diffusional transport in radial direction in Ba clusters | Reactions involved on Pt sites | Reactions involved on Ba sites

where ε_b ($m^3_{gas}/m^3_{reactor}$) is the bed porosity, C_i (mol_i/m^3_{gas}) is the gas-phase concentration of component i (NO, NO_2, O_2, H_2 and N_2), t (s) is time, F_v (m^3_{gas}/s) is the volumetric flow rate, A_r ($m^2_{reactor}$) is the surface area of the reactor, z ($m_{reactor}$) is

Table 5
Model parameters and constants

		Description
Catalyst parameters		
L_{Pt}	9.67	moles of Pt surface sites per m^3 reactor ($mol/m^3_{reactor}$)
$L_{Ba,total}$	2.06×10^3	moles of total Ba sites per m^3 reactor ($mol/m^3_{reactor}$)
$L_{Ba,surface}$	1.34×10^2	moles of Ba surface sites per m^3 reactor ($mol/m^3_{reactor}$)[a]
$L_{Ba,semi\text{-}bulk}$	4.01×10^2	moles of Ba semi-bulk sites per m^3 reactor ($mol/m^3_{reactor}$)[a]
$L_{Ba,bulk}$	1.53×10^3	moles of Ba bulk sites per m^3 reactor ($mol/m^3_{reactor}$)[a]
A_{Ba}	2.20×10^7	specific barium surface ($m^2_{Ba}/m^3_{reactor}$)
d_{Ba}	10×10^{-9}	diameter semi-bulk barium cluster (m_{Ba})
Reactor parameters		
ε_b	0.35	bed porosity ($m^3_{gas}/m^3_{reactor}$)
A_r	1.40×10^{-4}	surface area of the reactor ($m^2_{reactor}$)
F_v	3.54×10^{-5}	volumetric flow rate (m^3_{gas}/s)
$L_{reactor}$	1.50×10^{-2}	reactor length ($m_{reactor}$)
D_{eff}	3.64×10^{-15} [33]	diffusion coefficient ($m^3_{gas}/(m_{Ba}\ s)$)
$\varepsilon_{cluster}$	0.5	cluster porosity (m^3_{gas}/m^3_{Ba})
f	0.055	volume fraction ($m^3_{Ba}/m^3_{reactor}$)
NO oxidation parameters		
$K_{oxi\_equilibrium}$	2.05×10^1 [23]	NO oxidation equilibrium
k_{ox_f}	6.90×10^{-1} [23]	forward NO oxidation ($m^{4.5}_{gas}/(mol_i^{0.5}\ mol_{Pt}\ s)$)
k_{ox_b}	3.30×10^{-2} [23]	backward NO oxidation ($m^3_{gas}/(mol_{Pt}\ s)$)
Storage parameters		
Surface barium sites		
$k_{s\_NO_2,surface}$	1.60×10^5	NO_2 storage ($m^{7.5}_{gas}/(mol_i^{2.5}\ s)$)
$k_{s\_NO,surface}$	5.09×10^2	NO storage ($m^{7.5}_{gas}/(mol_i^{2.5}\ s)$)
$k_{s\_dis,surface}$	3.74×10^{-1}	nitrite oxidation ($m^6_{gas}/(mol_i^2\ s)$)
Semi-bulk barium sites		
$k_{s\_NO_2,semi\text{-}bulk}$	5.36×10^4	NO_2 storage ($m^{7.5}_{gas}/(mol_i^{2.5}\ s)\ mol_{Ba}/m^3_{Ba}$)
$k_{s\_NO,semi\text{-}bulk}$	2.68×10^{-1}	NO storage ($m^{7.5}_{gas}/(mol_i^{2.5}\ s)\ mol_{Ba}/m^3_{Ba}$)
$k_{s\_dis,semi\text{-}bulk}$	1.25×10^{-1}	nitrite oxidation ($m^6_{gas}/(mol_i^2\ s)\ mol_{Ba}/m^3_{Ba}$)
Bulk barium sites		
$k_{s\_NO_2,bulk}$	7.54×10^{-3}	NO_2 storage ($m^{7.5}_{gas}/(mol_i^{2.5}\ s)\ mol_{Ba}/m^3_{Ba}$)
Regeneration parameters		
Surface barium sites		
$k_{reg,nitrite,surface}$	5.96×10^{-2}	$Ba(NO_2)_2$ regeneration ($m^3_{gas}/(mol_i\ s)$)
$k_{reg,nitrate,surface}$	2.24×10^{-1}	$Ba(NO_3)_2$ regeneration ($m^3_{gas}/(mol_i\ s)$)
Semi-bulk barium sites		
$k_{reg,nitrite,semi\text{-}bulk}$	1.99×10^{-2}	$Ba(NO_2)_2$ regeneration ($m^3_{gas}/(mol_i\ s)\ mol_{Ba}/m^3_{Ba}$)
$k_{reg,nitrate,semi\text{-}bulk}$	7.48×10^{-1}	$Ba(NO_3)_2$ regeneration ($m^3_{gas}/(mol_i\ s)\ mol_{Ba}/m^3_{Ba}$)
Bulk barium sites		
$k_{reg,nitrate,bulk}$	1.96×10^{-1}	$Ba(NO_3)_2$ regeneration ($m^3_{gas}/(mol_i\ s)\ mol_{Ba}/m^3_{Ba}$)
Reduction parameters		
k_{red}	2.9×10^3	NO_x reduction ($m^6_{gas}/(mol_i^2\ s)$)

[a] Calculated with TGA result and 9 h lean/15 h rich cycling experiments.

the axial length, D_{eff} ($m^3_{gas}/(m_{Ba}\ s)$) is the effective gas diffusion coefficient, A_{Ba} ($m^2_{Ba}/m^3_{reactor}$) is the specific barium surface, ξ (m_{Ba}) is the radial direction in the barium clusters, L_{Pt} ($mol_{Pt}/m^3_{reactor}$) is the specific number of moles of active Pt surface sites, $R_{Pt,j}$ ($mol_i/(mol_{Pt}\ s)$) is the NO oxidation and reduction rate described in Eqs. (I) and (VII) in Table 4, and $L_{Ba,surf}$ ($mol_{Ba}/m^3_{reactor}$) is the specific number of moles of active barium surface sites. $R_{Ba\_surf,k}$ ($mol_i/(mol_{Ba}\ s)$) is the NO_x

storage and regeneration rate at barium surface sites and can be determined from the reaction equations (II)–(VI) mentioned in Table 4. Equation (2) calculates the time-dependent change of the different species on the surface barium sites,

$$\frac{\partial \theta_{\mathrm{m,surf}}}{\partial t} = \sum_k \upsilon_{i,k} R_{\mathrm{Ba\_surf},k}, \tag{2}$$

where $\theta_{\mathrm{m,surf}}$ (–) is the coverage of the surface barium sites and m denotes either $Ba(NO_2)_2$, $Ba(NO_3)_2$, or $BaCO_3$. The site balance for the surface barium sites is

$$\theta_{\mathrm{BaCO_3,surface}} = 1 - \theta_{\mathrm{Ba(NO_2)_2,surface}} - \theta_{\mathrm{Ba(NO_3)_2,surface}}. \tag{3}$$

Equation (4) represents the change in the concentration of the different gas-phase components as a function of time at each radial position for the semi-bulk and bulk barium sites,

$$\varepsilon_{\mathrm{cluster}} \frac{\partial C_i}{\partial t} = \frac{1}{\xi^2} \frac{\partial}{\partial \xi} \left(D_{\mathrm{eff}} \xi^2 \frac{\partial C_i}{\partial \xi} \right) + \sum_k \upsilon_{i,k} R_{\mathrm{Ba\_X},k}, \tag{4}$$

Accumulation of moles in gas phase in the Ba clusters | Diffusion in Ba clusters | Reactions involved on semi-bulk and bulk Ba sites

where $\varepsilon_{\mathrm{cluster}}$ ($m^3_{\mathrm{gas}}/m^3_{\mathrm{Ba}}$) is the porosity of the barium clusters, X is semi-bulk or bulk barium sites, and $R_{\mathrm{Ba\_X},k}$ ($\mathrm{mol}_i/(m^3_{\mathrm{Ba}}\,\mathrm{s})$) is the NO_x storage and regeneration rate for the semi-bulk and bulk sites that can be determined from the rate equations (II)–(VI) mentioned in Table 4. Equations (5) and (6) describe the time-dependent change of the different species on the semi-bulk and bulk barium sites, respectively,

$$\frac{L_{\mathrm{Ba,semi\text{-}bulk}}}{f} \frac{\partial \theta_{\mathrm{m,semi\text{-}bulk}}}{\partial t} = \sum_k \upsilon_{i,k} R_{\mathrm{Ba\_semi\text{-}bulk},k} \tag{5}$$

and

$$\frac{L_{\mathrm{Ba,bulk}}}{f} \frac{\partial \theta_{\mathrm{m,bulk}}}{\partial t} = \sum_k \upsilon_{i,k} R_{\mathrm{Ba\_bulk},k}, \tag{6}$$

where $L_{\mathrm{Ba,semi\text{-}bulk}}$ and $L_{\mathrm{Ba,bulk}}$ ($\mathrm{mol_{Ba}}/m^3_{\mathrm{reactor}}$) are the specific number of moles of active semi-bulk and bulk barium sites, f ($m^3_{\mathrm{Ba}}/m^3_{\mathrm{reactor}}$) is the volume fraction, $\theta_{\mathrm{m,semi\text{-}bulk}}$ (–) is the coverage of the semi-bulk barium sites, and $\theta_{\mathrm{m,bulk}}$ (–) is the coverage of the bulk barium sites. The site balance for the semi-bulk and bulk barium sites is shown in Eqs. (7) and (8). In accordance with literature, NO_x is only stored as nitrates on bulk barium sites [31,32],

$$\theta_{\mathrm{BaCO_3,semi\text{-}bulk}} = 1 - \theta_{\mathrm{Ba(NO_2)_2,semi\text{-}bulk}} - \theta_{\mathrm{Ba(NO_3)_2,semi\text{-}bulk}}, \tag{7}$$

$$\theta_{\mathrm{BaCO_3,bulk}} = 1 - \theta_{\mathrm{Ba(NO_3)_2,bulk}}. \tag{8}$$

The initial and boundary conditions are as follows:
$C_i = 0$, $\theta_{\mathrm{Ba(NO_3)_2},y} = 0$, and $\theta_{\mathrm{Ba(NO_2)_2},y} = 0$ at $t = 0$, where y is surface, semi-bulk, or bulk barium sites;

$$C_i = C_{\mathrm{in}}, \quad \text{at } t > 0 \text{ and } z = 0;$$

and

$$\frac{\partial C_{i,z,\xi}}{\partial \xi} = 0, \quad \text{at } \xi = 0 \text{ and at any } t.$$

The system of equations is solved using gPROMS (Process Systems Enterprise) software.

5. Modeling results and discussion

5.1. Lean/rich cycling in the order of hours

Fig. 6 shows the results from the model (dashed lines) together with the measured outlet NO and NO_2 concentrations (solid lines) for the 9-h lean phase with 0.2 vol% inlet NO. The model is well able to describe the three different time periods in the lean phase. The first period shows complete NO_x uptake during the first 6.2 min. Figs. 7a–7e show that during this period, NO storage occurs mainly on the surface barium sites, in the form of nitrites. As the storage process proceeds, the surface coverage of nitrite and nitrates increases (Fig. 7a) and NO breakthrough in the gas phase is seen. This is the start of the second period. The formation of surface barium nitrites continues showing a maximum coverage at 8.4 min (Fig. 7a). At this stage, all of the surface $BaCO_3$ sites have been converted to nitrites and nitrates. After 8.4 min, the surface nitrites coverage begins to decline, while at the same time the surface barium nitrate coverage increases. This indicates that nitrites are oxidized into nitrates with NO_2 as oxidizing agent. As a result, delay in NO_2 breakthrough and increase in NO concentration occur, as shown in Fig. 6. From this point onward, semi-bulk barium sites participate in the NO and NO_2 storage process (Figs. 7b–7d), showing barium nitrite and nitrate coverage. The third period begins after 65 min, during which the surface barium sites are entirely occupied with $Ba(NO_3)_2$ (Fig. 7a). The NO_x storage rate decreases, because only semi-ulk and bulk barium sites are available and diffusion starts to play a major role. After 67 min, all semi-bulk $BaCO_3$ sites have been replaced by $Ba(NO_2)_2$ and $Ba(NO_3)_2$ (Figs. 7b–7d). However, as the lean phase proceeds, the barium nitrate coverage of the semi-bulk sites increases, coinciding with a decrease of the barium nitrite coverage. After 200 min, the semi-bulk sites are fully covered with nitrates (Figs. 7b–7d). Only a fraction of the bulk barium sites still participates in NO_x storage, showing negligible reactivity (Fig. 7e). Even after 9 h of lean exposure, the bulk

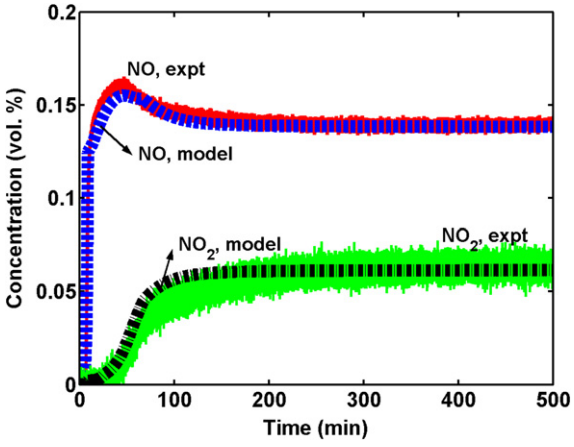

Fig. 6. Simulated and measured lean NO and NO_2 outlet concentrations. For experimental conditions, see Fig. 1.

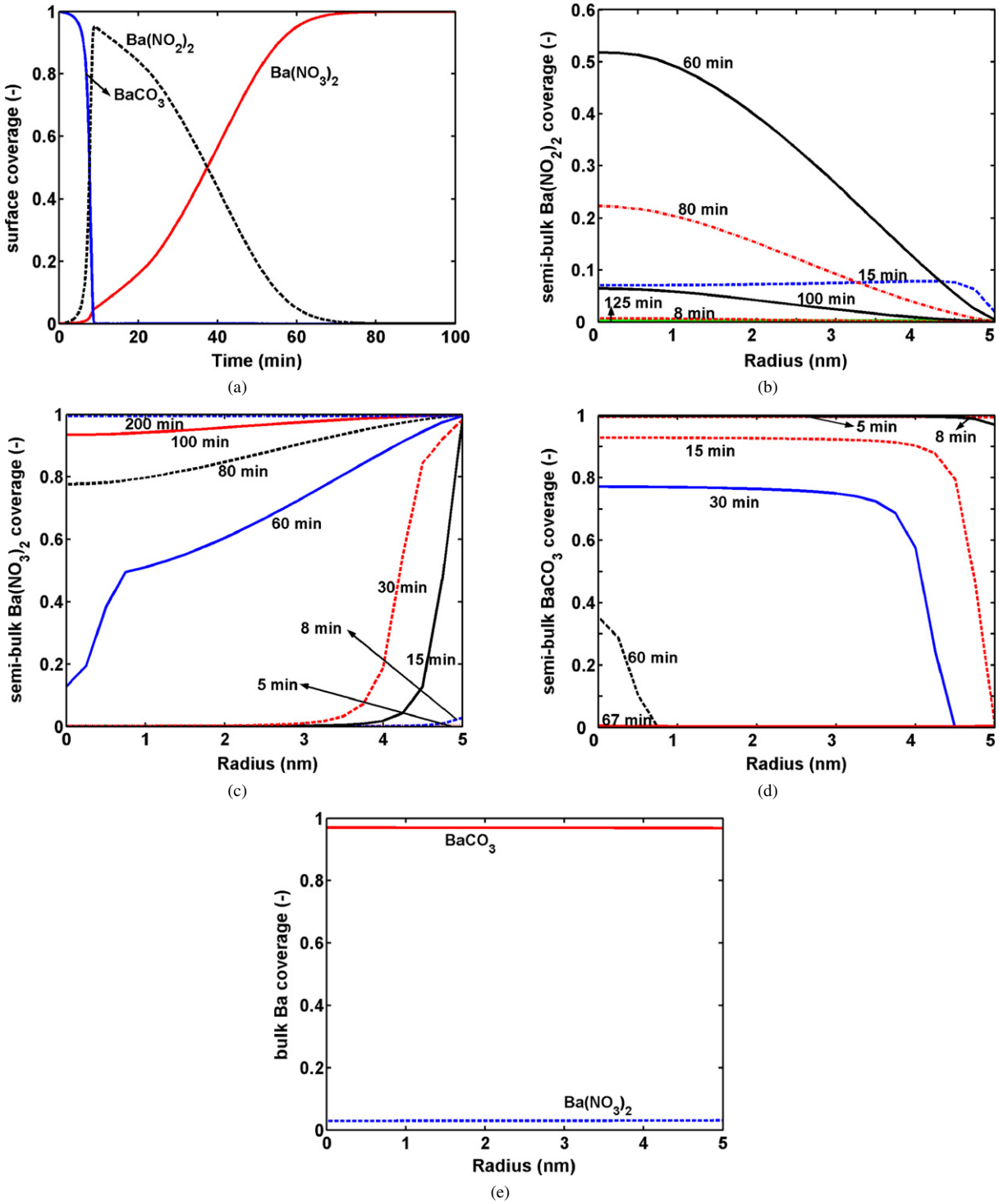

Fig. 7. Simulated coverages during lean exposure: (a) coverage of surface barium sites, (b) $Ba(NO_2)_2$ coverage of semi-bulk barium sites, (c) $Ba(NO_3)_2$ coverage of semi-bulk barium sites, (d) $BaCO_3$ coverage of semi-bulk barium sites, (e) $Ba(NO_3)_2$ and $BaCO_3$ coverage of bulk barium sites after 9 h lean exposure. For experimental conditions, see Fig. 1.

coverage consists mainly of $BaCO_3$. As a result, the NO_x storage process ends as the surface and semi-bulk sites have been fully converted to nitrates.

Under fuel-rich conditions, N_2 formation and NO desorption were experimentally observed (Fig. 8). The model adequately describes the NO desorption. The measured N_2 concentration initially shows a lower concentration before it increases to 0.16 vol%. A possible reason for this might be that part of the H_2 is used for reduction of the Pt sites, resulting in less H_2 available for NO_x reduction. The model does not take this into account. As a result, the simulation immediately shows a N_2 concentration of 0.16 vol%. Consequently, more nitrate will be reduced in the same time span in the model compared with the experimental results. Therefore, the simulation results show a

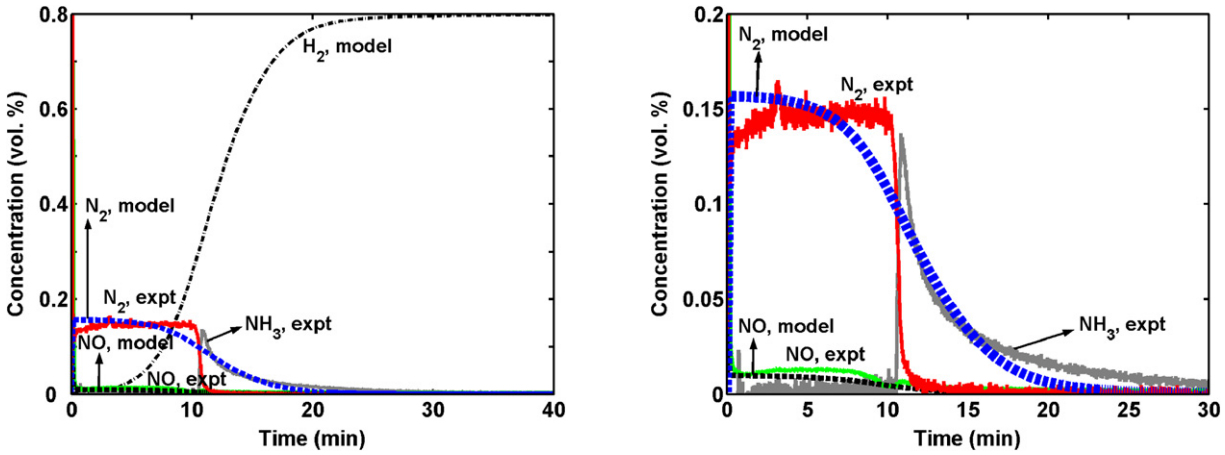

Fig. 8. (a) Simulated and measured rich NO, H_2 and N_2 outlet concentrations. For experimental conditions, see Fig. 1. (b) Zoom in of (a).

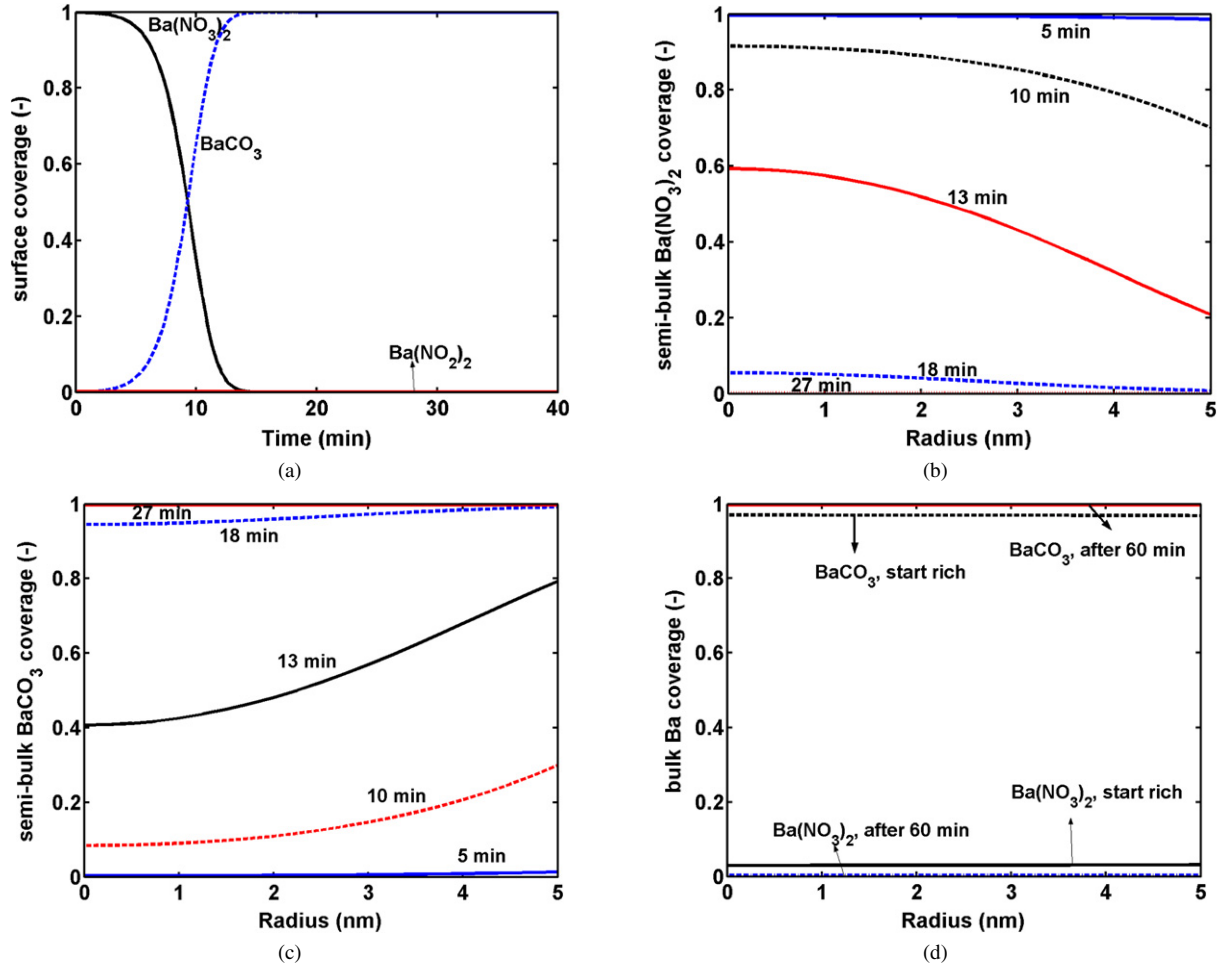

Fig. 9. Simulated coverages during rich exposure: (a) coverage of surface barium sites, (b) $Ba(NO_3)_2$ coverage of semi-bulk barium sites, (c) $BaCO_3$ coverage of semi-bulk barium sites, (d) $Ba(NO_3)_2$ and $BaCO_3$ coverage of bulk barium sites. For experimental conditions, see Fig. 1.

decreased N_2 concentration after 8 min, compared with 11 min for the experimental data. Simulations show that initially, all H_2 is completely consumed. As the rich phase proceeds, incomplete consumption of H_2 is seen, resulting in excess H_2. It can be observed experimentally that this leads to NH_3 formation after 11 min. The NH_3 concentration slowly decreases with time. NH_3 production is not modeled, because NH_3 is not observed at cycle timings close to automotive conditions. However, the simulated N_2 concentration shows the same characteristics as the experimentally observed $N_2 + 2NH_3$ signal. Figs. 9a–9d show the coverages of the surface, semi-bulk and bulk barium sites. At first, the surface nitrates are reduced and surface $BaCO_3$ is

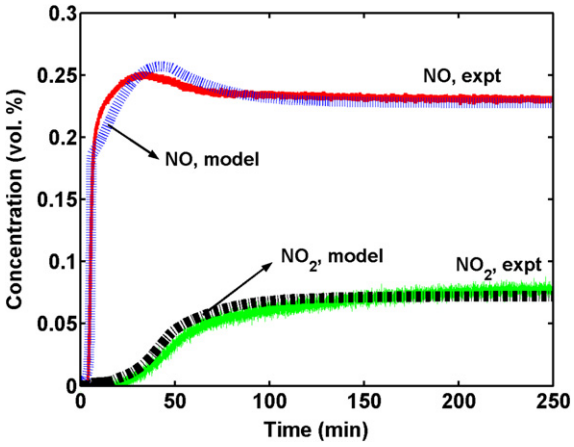

(a)

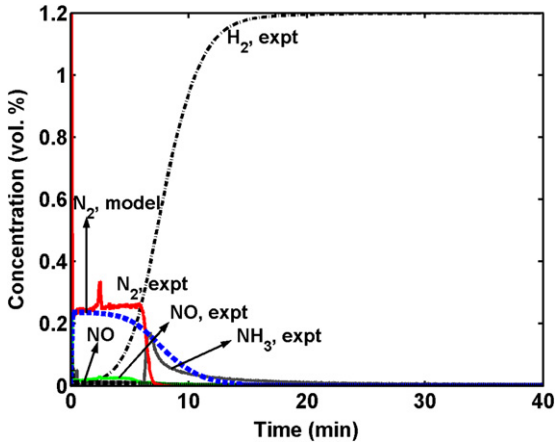

(b)

Fig. 10. (a) Simulated and measured lean NO and NO_2 outlet concentrations at cyclic steady state. Lean phase: 0.3 vol% NO, 4 vol% O_2, 10 vol% CO_2 and 1 vol% Ar, 9 h. (b) Simulated and measured rich NO, H_2 and N_2 outlet concentrations at cyclic steady state. Rich phase: 1.2 vol% H_2, 10 vol% CO_2 and 1 vol% Ar, 15 h. $T = 573$ K.

formed (Fig. 9a). After 5 min, the semi-bulk sites participate in the regeneration process (Figs. 9b and 9c). The surface sites are completely regenerated after 17 min. Complete regeneration for the semibulk sites occurs after 27 min.

Fig. 10a shows the lean NO and NO_2 concentrations for the higher inlet NO concentration (0.3 vol%). The model is able to simulate the complete NO_x uptake, as well as the NO and NO_2 breakthrough timings. There is a small discrepancy between the model and the experimental results for the NO profile. Literature reports indicate that the NO oxidation rate shows a negative first order with respect to NO_2 concentration [34]. This inhibiting effect is not incorporated into the model, possibly leading to the small discrepancy observed. Fig. 10b shows that the model can also capture NO_x desorption during rich exposure with higher H_2 concentration (1.2 vol%). The simulated N_2 profile closely corresponds to the measured $N_2 + 2NH_3$ signal.

5.2. *Lean/rich cycling in the order of seconds*

Fig. 11 shows the model prediction and experimental results of transient reactor operation for 20 lean/rich cycles with 240-s

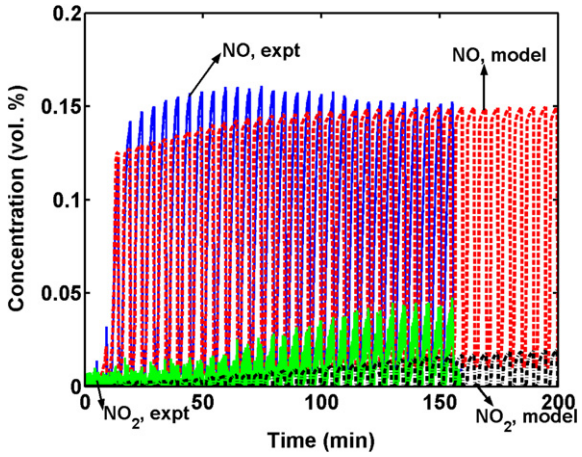

Fig. 11. Simulated and measured NO, NO_2 and N_2 outlet concentrations at $T = 573$ K. Lean phase: 240 s, 0.2 vol% NO, 4 vol% O_2, 10 vol% CO_2 and 1 vol% Ar. Rich phase: 60 s, 0.8 vol% H_2, 10 vol% CO_2 and 1 vol% Ar. For modeling purpose 0.6 vol% H_2 was used in the rich phase. See text for explanation.

lean and 60-s rich phases. As mentioned earlier, during the first few minutes of rich exposure, part of the H_2 likely is used for the reduction of Pt sites. This leads to less H_2 available for NO_x reduction. Therefore, simulation results show initially a higher N_2 concentration, as observed experimentally. For this reason, the inlet H_2 concentration used in modeling the transient experiments was set to 0.6 vol%. The first two storage/reduction cycles show complete NO_x uptake. Fig. 12a shows that NO_x is initially stored on surface barium sites in the form of nitrites. During the catalyst regeneration period, N_2 formation and NO desorption are observed. No NH_3 formation is seen, and the reverse WGS reaction does not take place. NO_x stored during lean exposure is not completely reduced during the subsequent rich period, as shown in Fig. 12a. As a result, nitrites and nitrates accumulate on the barium sites, and part of the barium will be inactive for NO_x storage and reduction. After two lean/rich cycles, NO breakthrough during lean exposure can be seen. The NO storage continues with the involvement of semi-bulk barium sites (Figs. 12b–12d). Meanwhile, NO_2 is consumed in oxidizing surface nitrites into nitrates and by getting stored on semi-bulk barium sites. After a number of lean/rich cycles, NO_2 breakthrough can be seen. The experimental results show that the cyclic steady state is not reached. Simulation results (Figs. 12a–12e) illustrate that as lean/rich cycling proceeds, more nitrate accumulates in the catalyst until all semi-bulk barium sites have been filled. At that moment, the cyclic steady state has been reached. At the cyclic steady state, only surface barium sites participate in the NO_x storage/reduction process. Bulk barium sites show negligible activity toward NO_x storage (Fig. 12e).

At real-life application, rapid alternation of NO_x storage and reduction phases takes place in the order of seconds. The aforementioned model results suggest that in this case, surface barium sites are decisive, and only a fraction of the total barium sites are active in NO_x storage. As a result, NO_x breakthrough in the lean phase is observed. Restoring the maximum NO_x storage capacity implies regeneration of both surface and semi-

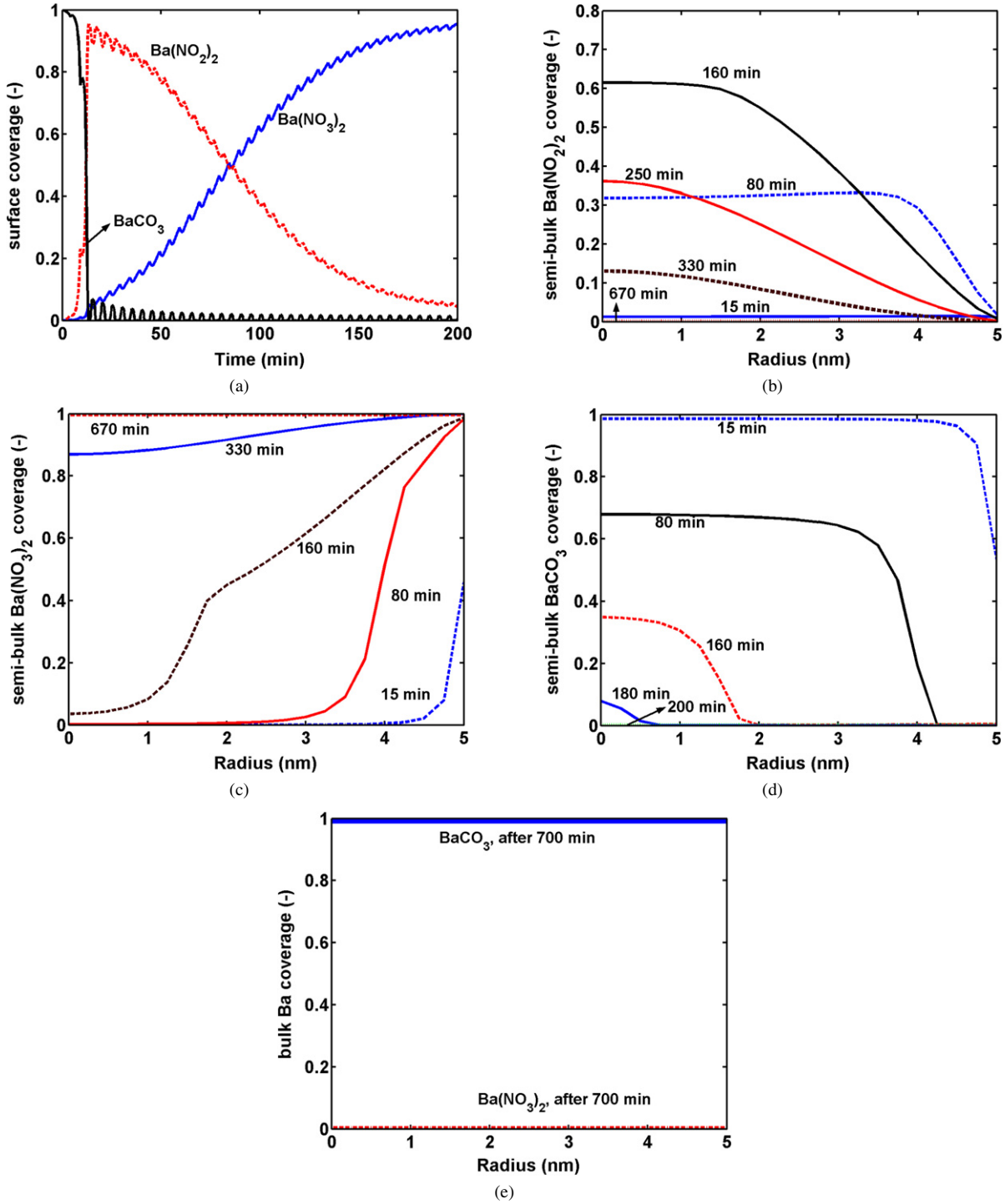

Fig. 12. Simulated coverages during transient reactor operation: (a) coverage of surface barium sites, (b) $Ba(NO_2)_2$ coverage of semi-bulk barium sites, (c) $Ba(NO_3)_2$ coverage of semi-bulk barium sites, (d) $BaCO_3$ coverage of semi-bulk barium sites, (e) $Ba(NO_3)_2$ and $BaCO_3$ coverage of bulk barium sites. For experimental conditions, see Fig. 11.

bulk barium sites. Consequently, considerable breakthrough of the reducing agent can occur. The present model can be used to simulate and optimize the transient operating conditions.

6. Conclusion

A global reaction kinetic model has been developed based on a multiple–storage site mechanism for the NO_x storage/reduction process in the presence of CO_2. The model considers that fast NO_x storage occurs at surface barium sites, which is determined by the reaction kinetics. Slow NO_x storage occurs at semi-bulk sites, where diffusion plays a major role. Bulk barium sites show negligible reactivity toward NO_x storage. It is assumed that surface, bulk, and semi-bulk sites differ not only in physical appearance, but also in chemical reactivity. Surface and semi-bulk sites correspond to a dispersed

LT barium phase and bulk barium sites with crystalline HT-$BaCO_3$ sites. The distribution of these sites is obtained from a TGA experiment with fresh catalyst showing that around 35% (w/w) of total barium is present as LT barium sites and 65% is present as HT-$BaCO_3$. This agrees well with results obtained from 9-h/15-h lean/rich cycling experiments in combination with XRD measurements. The barium utilization after 9 h of lean exposure is about 32% of the total barium present. XRD measurements show that HT-$BaCO_3$ is inactive in the NO_x storage process in the presence of CO_2.

The model demonstrates that the initial complete NO_x uptake can be ascribed mainly to NO storage on surface barium sites in the form of nitrites. As the surface coverage increases, NO breakthrough can be seen. The NO storage process continues with the involvement of semi-bulk barium sites but at a lower rate due to diffusion limitations. Meanwhile, NO_2 is consumed in oxidizing surface nitrites into nitrates and is stored on semi-bulk barium sites. As a result, a delay in NO_2 breakthrough can be seen. It appears that the bulk barium sites show negligible activity toward NO_x storage. The model can also describe NO_x desorption during rich exposure. Experimental results show N_2 formation initially, followed by NH_3 production. NH_3 formation is not seen for cycle timings close to automotive conditions. For this reason, NH_3 formation was not modeled. The simulated N_2 signal describes the measured $N_2 + 2NH_3$ characteristics. The model is able to describe experiments with higher NO and H_2 inlet concentration as well as transient reactor experiments with 240-s lean and 60-s rich-cycle timings.

Acknowledgments

This project was financed by the Dutch Technology Foundation (STW). Support of PSA, Ford, Engelhard, PD&E Automotive solutions, Shell, IPCOS, EP Controls, and Toyota is gratefully acknowledged, as are Dr. I. Babich for the TPD and M. Hendrix for the XRD measurements.

References

[1] S. Matsumoto, Catal. Today 29 (1996) 43.
[2] P. Engstrom, A. Amberntsson, M. Skoglundh, E. Fridell, G. Smedler, Appl. Catal. B Environ. 22 (1999) L241.
[3] W.S. Epling, L.E. Campbell, A. Yezerets, N.W. Currier, J.E. Parks, Catal. Rev. 46 (2004) 163.
[4] F. Prinetto, G. Ghiotti, I. Nova, L. Castoldi, L. Lietti, E. Tronconi, P. Forzatti, Phys. Chem. Chem. Phys. 5 (2003) 4428.
[5] N.W. Cant, M.J. Patterson, Catal. Today 73 (2002) 271.
[6] F. Laurent, C.J. Pope, H. Mahzoul, L. Delfosse, P. Gilot, Chem. Eng. Sci. 58 (2003) 1793.
[7] L. Lietti, P. Forzatti, I. Nova, E. Tronconi, J. Catal. 204 (2001) 175.
[8] J. Despres, M. Koebel, O. Krocher, M. Elsener, A. Wokaun, Appl. Catal. B Environ. 43 (2003) 389.
[9] B. Westerberg, E. Fridell, J. Mol. Catal. A Chem. 165 (2001) 249.
[10] L. Castoldi, I. Nova, L. Lietti, P. Forzatti, Catal. Today 96 (2004) 43.
[11] E. Fridell, H. Persson, B. Westerberg, L. Olsson, M. Skoglundh, Catal. Lett. 66 (2000) 71.
[12] P. Broqvist, H. Gronbeck, E. Fridell, I. Panas, Catal. Today 96 (2004) 71.
[13] C. Sedlmair, K. Seshan, A. Jentys, J.A. Lercher, J. Catal. 214 (2003) 308.
[14] D. James, E. Fourre, M. Ishii, M. Bowker, Appl. Catal. B Environ. 45 (2003) 147.
[15] W.S. Epling, J.E. Parks, G.C. Campbell, A. Yezerets, N.W. Currier, L.E. Campbell, Catal. Today 96 (2004) 21.
[16] H. Mahzoul, J.F. Brilhac, P. Gilot, Appl. Catal. B Environ. 20 (1999) 47.
[17] X. Chen, J. Schwank, J. Li, W.F. Schneider, C.T. Goralski, P.J. Schmitz, J. Mater. Chem. 15 (2005) 366.
[18] M. Piacentini, M. Maciejewski, A. Baiker, Appl. Catal. B Environ. 59 (2005) 187.
[19] X. Chen, J. Schwank, J. Li, W.F. Schneider, C.T. Goralski, P.J. Schmitz, Appl. Catal. B Environ. 61 (2005) 164.
[20] M. Piacentini, M. Maciejewski, A. Baiker, Appl. Catal. B Environ. 60 (2005) 265.
[21] L. Olsson, E. Fridell, M. Skoglundh, B. Andersson, Catal. Today 73 (2002) 263.
[22] J.I. Theis, U. Gobel, M. Kogel, T.P. Kreuzer, D. Lindner, E. Lox, L. Ruwisch, SAE Technical Paper, Special Edition SP-1676 (2002) 1.
[23] L. Olsson, R.J. Blint, E. Fridell, Ind. Eng. Chem. Res. 44 (2005) 3021.
[24] U. Tuttlies, V. Schmeisser, G. Eigenberger, Top. Catal. 30/31 (2004) 187.
[25] J.S. Hepburn, E. Thanasiu, D.A. Dobson, W.L. Watkins, SAE Technical Paper 962051 (1996).
[26] W.S. Epling, G.C. Campbell, J.E. Parks, Catal. Lett. 90 (2003) 45.
[27] I. Nova, L. Castoldi, L. Lietti, E. Tronconi, P. Forzatti, Catal. Today 2747 (2002) 1.
[28] S. Balcon, C. Potvin, L. Salin, J.F. Tempere, G. Djega-Mariadassou, Catal. Lett. 60 (1999) 39.
[29] A. Amberntsson, H. Persson, P. Engstrom, B. Kasemo, Appl. Catal. B Environ. 31 (2001) 27.
[30] C.M.L. Scholz, V.R. Gangwal, J.H.B.J. Hoebink, J.C. Schouten, Appl. Catal. B Environ. (2006), doi: 10.1016/j.apcatb.2006.01.032.
[31] F. Rodrigues, L. Juste, C. Potvin, J.F. Tempere, G. Blanchard, G. Djega-Mariadassou, Catal. Lett. 72 (2001) 59.
[32] P.J. Schmitz, R.J. Baird, J. Phys. Chem. B 106 (2002) 4172.
[33] F. Dong, A. Suda, T. Tanabe, Y. Nagai, H. Sobukawa, H. Shinjoh, M. Sugiura, C. Descorme, D. Duprez, Catal. Today 90 (2004) 223.
[34] S.S. Mulla, N. Chen, W.N. Delgass, W.S. Epling, F.H. Ribeiro, Catal. Lett. 100 (2005) 267.